Dendrite Initiation and Propagation in Lithium Metal Solid-State Batteries

Ziyang Ning[1,2†], Guanchen Li[3,4,5†], Dominic L. R. Melvin[1,5†], Yang Chen[1,6], Junfu Bu[1,5], Dominic Spencer-Jolly[1,5], Junliang Liu[1], Bingkun Hu[1], Xiangwen Gao[1,5], Johann Perera[1], Chen Gong[1], Shengda D. Pu[1], Shengming Zhang[1], Boyang Liu[1,5], Gareth O. Hartley[1,5], Andrew Bodey[7], Richard I. Todd[1], Patrick S. Grant[1,5], David E. J. Armstrong[1,5], T. James Marrow[1]*, Charles W. Monroe[3,5]*, & Peter G. Bruce[1,5,8]*

1. Department of Materials, University of Oxford, Oxford, UK
2. Fujian Science & Technology Innovation Laboratory for Energy Devices (21C Lab), Ningde 352100, China
3. Department of Engineering Science, University of Oxford, Oxford, UK
4. James Watt School of Engineering, University of Glasgow, Glasgow, UK
5. The Faraday Institution, Harwell Campus, Didcot, UK
6. Department of Mechanical Engineering, University of Bath, Bath, UK
7. Diamond Light Source, Harwell Campus, Didcot, UK
8. Department of Chemistry, University of Oxford, Oxford, UK

† These authors contributed equally

*Correspondence: james.marrow@materials.ox.ac.uk; charles.monroe@eng.ox.ac.uk; peter.bruce@materials.ox.ac.uk

Abstract

All-solid-state batteries with a Li anode and ceramic electrolyte have the potential to deliver a step change in performance compared with today's Li-ion batteries[1,2]. However, Li dendrites (filaments) form on charging at practical rates, penetrate across the ceramic electrolyte leading to short-circuit and cell failure[3,4]. Previous models of dendrite penetration have generally focused on a single process for dendrite initiation and propagation, with Li driving the crack at its tip[5–9]. Here we show that initiation and propagation are separate processes. The former arises from filling sub-surface pores with Li via microcracks that connect the pores

to the surface. Once filled, further charging builds pressure in the pores due to slow extrusion of Li, (viscoplastic flow) back to the surface, leading to cracking. In contrast, dendrite propagation occurs by wedge-opening, with Li driving the dry crack from the rear not the tip. Whereas initiation is determined by the local (microscopic) fracture strength at the grain boundaries, the pore-size, pore population density and current density, propagation depends on the (macroscopic) fracture toughness of the ceramic, the length of the Li dendrite (filament) that partially occupies the dry crack, current density, stack pressure and the charge capacity accessed during each cycle. Lower stack pressures suppress propagation, markedly extending the number of cycles before short circuit in cells where dendrites have initiated.

Main

The ceramic electrolyte microstructure obtained from operando X-ray computed tomography (XCT) and focused ion beam scanning electron microscopy (FIB-SEM), in combination with the local (grain boundary) fracture strength from microcantilever measurements, is used to predict the critical current for initiation. Stack pressures of a few MPa do not affect the critical initiation current, but values above 50 MPa, typical in the literature[10–12], lower it. The electric-field and current-density enhancement previously suggested to occur in sub-surface pores[13] is reduced when pores are close together, which also impacts critical current predictions.

In practical cells pressures at the Li anode may be applied externally or develop internally. By varying stack pressure, we can investigate systematically the effect of pressurising Li anodes during charge on crack propagation. Although Li filaments elongate within a dry crack during plating and shrink during stripping, stack pressure induces net filament elongation on each cycle. We identify a critical length of lithium filling within a dry crack that causes the crack tip to propagate. Moderate stack pressures (7 MPa) cause Li filaments to reach this critical propagation length after a few cycles at moderate current density. By lowering stack pressure, cycle life before short-circuit can be extended substantially. A Li_6PS_5Cl solid electrolyte cell with a Li anode, cycled at a plating current density of 4.0 mA/cm^2 and stripped at 0.05 mA/cm^2 (for a capacity of 0.5 mAh/cm^2 per half cycle), failed after 35 cycles under 7 MPa of stack pressure, whereas the same cell under atmospheric pressure (0.1 MPa) can have its cycling prolonged 5-fold, avoiding short-circuit for 170 cycles. The results demonstrate that dendrites

can be inhibited by supressing their propagation. Inhibiting dendrite penetration can be based on suppressing either initiation or propagation, the former by increasing the local fracture strength, as well as minimising pore size and controlling pore proximity, and the latter by maximising electrolyte fracture toughness and minimising pressure on the Li anode.

Operando X-ray computed tomography

We used continuous *operando* XCT scanning with vastly improved time resolution, compared with previous studies[14,15] to follow the initiation and propagation of cracks during constant-current plating. XCT data are reported on an argyrodite sample sintered under identical conditions as the material used to determine mechanical properties, ensuring consistency of the parameters used for modelling. Lithium plating first creates a spallation at the edge of the metal electrode, followed by formation of a transverse crack that propagates across the electrolyte to the other electrode, Fig 1b. This process accords with our earlier studies[3] the crack reaches the other electrode before the Li dendrite – indicated by the lack of short circuit until after step (vii), Fig 1a. Li also plates on the working electrode, which thickens as a result, not only in the crack. To demonstrate Li in the transverse crack reaching the counter electrode is responsible for the short circuit and not any other Li filaments elsewhere, we show XCT results in Fig. S8 where we follow the progression of Li along the crack. The short circuit occurs at the point where the Li reaches the counter electrode.

Images (i) to (iv) in Fig 1c reveal the earliest morphological changes. By 7 m 20 s, a piece of argyrodite has been spalled out, detaching from the bulk electrolyte, Fig 1c(iii). The image before detachment, Fig 1c(ii), shows that the fracture pathway of the spallation connects pre-existing pores 20 to 50 µm from the interface (two are indicated by yellow arrows). Comparing Fig 1c(i) & (ii) indicates that the pre-existing pores enlarge as plating proceeds, suggesting they are being filled with Li. Pre-existing pores are also observed along the fracture pathway of the transverse crack, marked by red arrows in Fig 1c(iii).

The deposition of Li in sub-surface pores was further demonstrated by two techniques. A FIB-SEM cross-sectional image showing the pores was combined with SIMS analysis to identify Li, Fig 1d. The results show a subsurface pore filled with Li metal within the Li_6PS_5Cl electrolyte after plating. Second, sub-surface Li metal was detected by etching a Li_6PS_5Cl disk after plating,

removal from the cell and etching with LiOH solution while concurrently performing mass spectrometry, Fig 1e, as detailed in the Methods. The lag in H_2 detection is consistent with Li being primarily deposited in subsurface pores.

Overall, the results in Fig 1 suggest two stages of dendritic failure, crack initiation and crack propagation.

Crack initiation based on pore filling

The model, Fig. 2, simulates a sub-surface pore, as a spherical cavity, connected to the electrolyte's exterior by a pre-existing micro-crack, modelled as a cylindrical void space normal to the electrode surface. On plating, Li deposits first at the top surface of the micro-crack, progressively filling it and the pore, Fig 2a. It has been suggested that that Li nucleation can occur in sub-surface pores due to some electronic conductivity[13,16,17]. Whatever the process of pre-filling, the entire pore/crack assembly fills early on initial plating, leading to a lithium-filled configuration shown in Fig 2b. Further Li deposition occurs across the entire Li/electrolyte interface (pore and microcrack surface). Because the defect is already occupied, this deposition induces a strain within the defect structure, which is accompanied by a pressure build-up. The net effect is Li extrusion back along the microcrack, to accommodate the freshly deposited Li. Because lithium metal is a viscoplastic solid, its motion along the narrow microcrack is analogous to a non-Newtonian pipe flow and is largely controlled by the current density in the subsurface pore. At sufficiently high plating rates, the high pressure drop associated with this viscoplastic flow is capable of inducing electrolyte fracture. Fracture near subsurface pores associated with lithium flow through microcracks thus underpins the initiation process.

Estimation of the critical current density for dendrite crack initiation, CCD_{init}, necessitates viscoplastic property data for Li metal, as well as a fracture criterion for the solid electrolyte. Recent experiments quantifying the power-law creep of Li have been incorporated into the model as detailed in the Supplementary Information[18,19]. The fracture criterion requires information about how the ceramic responds to microscopically applied stress[20]. Such local fracture characteristics cannot be quantified accurately by standard mechanical tests, which sample macroscopic properties averaged across multiple grains[21]. Instead, the local fracture

strength of grain boundaries in the argyrodite was measured by microcantilever bending, as depicted in Fig 2c (see also Methods and Fig S19). The smoothness of the microcantilever fracture surfaces suggests intergranular fracture (see Figure S20), although this is indirect evidence and not conclusive. The situation may be different for oxides, which have quite different mechanical properties.

The model for crack initiation and accompanying calculations are detailed in the Supplementary Information. Results are presented graphically in Fig 2d & e. Using the pore dimensions and proximity to the surface from XCT (Fig 1), as well as FIB-SEM images (Fig S10), calculations showing how hydrodynamic pressure in the pore depends on the plating current density are presented in Fig 2d. The critical current density for initiation (CCD_{init}) is determined by the local fracture strength, shown by the dashed horizontal line in Fig 2d. At a sufficiently high current density, the pore pressure exceeds the local fracture strength, inducing fracture.

The current density at the pores is a balance of two factors. The field enhancement at the tips of a conductor effect[22] acts to increase the current density while the presence of neighbouring pores spreads the current, both are important in relating the overall applied current density to that at the pores, see Figure S2.

The turquoise line in Fig. 2d, represents a microcrack without a pore. The other lines in Fig 2d shows how the presence of pores and their increasing size induces a higher extrusion rate of Li at a given applied current density, and hence higher pressure, explaining why subsurface pores are the weaknesses most likely to initiate cracks. Fig 2e shows that decreasing pore size or increasing the local fracture strength increases CCD_{init}.

Based on the size, population density, and surface proximity of pores, and the local fracture strength determined for Li_6PS_5Cl with XCT, SEM and microcantilever measurements (see SI), the model predicts that CCD_{init} is ~1.0 mA/cm^2. In line with typical experimental values[4,23].

Crack propagation based on wedge opening

The observations of dry cracks that lengthen and widen on plating, wherein Li fills the base but is absent from the tip, suggests a wedge-opening propagation mechanism.

The images in Figures 1b and S12 indicate that dendrite propagation across the electrolyte occurs within an approximately planar crack, represented schematically in Fig 3a. Lithium plating occurs along the crack interior that contact the crack-filling metal. Li deposition at the lateral interfaces (blue surfaces in Fig 3b) induces a pressure build-up and a resulting viscoplastic flow that drives motion of the dendrite tip into the void space and Li extrusion back into the bulk Li anode. Applied stack pressure enhances Li flow toward the crack tip and inhibits extrusion. Extrusion only occurs when the pressure induced by the plating current – which is generally non-uniform along the length of the dendrite – exceeds the stack pressure.

By modelling the stress field near the dry crack tip, one can calculate the strain energy release rate, i.e. the energy available to lengthen the crack, quantified by the J-integral[24]. The criterion for fracture, and therefore crack propagation, is determined by comparing the calculated J-integral to the critical strain energy release rate required for propagation, a material property dependent on the electrolyte's fracture toughness, Young's modulus and Poisson's ratio. The fracture toughness and Young's modulus of the Li_6PS_5Cl solid electrolyte were measured by nanoindentation, as described in the Methods. The propagation model is detailed in the Supplementary Information.

The *operando* XCT micrograph in Fig 1b (iv) shows a crack in the process of propagation, which has initiated but not yet reached the counter electrode. From its approximate dimensions, 200 µm long and 2 µm wide, the stress field at the crack tip was modelled quasi-statically during the continuous growth of the Li dendrite, for a current density of 3.0 mA/cm^2 (typical of a practical charging rate and commensurate with the current used to collect the XCT in Fig 1), see SI for details. As the Li dendrite grows in the crack, the strain energy release rate (J-integral) rises super-linearly with the Li dendrite length. Increasing area of Li/electrolyte contact within a dendrite increases both the flux of Li into the dendrite and the area of the electrolyte under stress from pressurised crack-filling Li, Fig 3c. Since pressures within the dendrite depend on the Li flow, the magnitude of the J-integral for a given dendrite length is greater for higher current densities, as shown for a fixed dendrite length of 115 µm in Figure 3d.

The critical J-integral for crack propagation in Li_6PS_5Cl is shown by the black dashed lines in Figures 3c & d. Fig 3c shows the effect of dendrite length: for a plating current density of 3.0 mA/cm^2 under 7 MPa stack pressure, the Li only needs to fill half the crack length (~115 µm)

before the dry crack lengthens, consistent with the wedge-opening propagation seen in Figure 1 and our previous work[3]. When stack pressure is reduced, dendrites must be longer to propagate the dry crack. For a dendrite length of 115 μm and stack pressure of 7 MPa, crack propagation occurs at 2.4 mA/cm^2, whereas removal of the stack pressure increases this significantly, to 4.2 mA/cm^2, Fig 3d. Stack pressure has a major influence on how lithium deposition drives the growth of dry cracks.

Crack propagation can be inhibited by toughening the electrolyte[21,25], Fig 3e, since increasing fracture toughness increases the J-integral required for crack extension. With a higher fracture toughness, crack propagation requires higher current densities or longer Li dendrites, Fig 3e.

When does propagation lead to a short circuit?

The capacity plated and stripped per half cycle and the stack pressure affect whether crack propagation will result in a short-circuit. Taking the 200 μm long, 2 μm wide crack from the XCT section shown in Fig 1b (iv), simulations to determine the net Li dendrite growth after a single cycle as a function of capacity were performed for applied stack pressures of 7 MPa, 1 MPa, and 0 MPa, Fig 4a. Simulated dendrite length during repeated cycling is shown in Fig 4b. The net dendrite-length change during a plating/stripping cycle over a given capacity varies with the applied stack pressure. Stack pressure promotes Li flow towards the counter electrode and inhibits extrusion, resulting in greater net growth. Cycling at a stack pressure of 7 MPa (orange) results in a substantial cumulative length change that soon drives crack propagation (dashed black line in Fig 4b), while lower stack pressures reduce the net propagation markedly, Fig 4b. For a given stack pressure and current density, the number of cycles to short circuit depends on the capacity per half cycle and the electrolyte thickness. This effect of stack pressure on the net accumulation of Li in the electrolyte on cycling was further demonstrated experimentally by quantifying the amount of Li remaining within the solid electrolyte after cycling at different stack pressures using mass spectrometry (see Figure S13). Higher pressures and cycle numbers lead to more residual Li in the SE after stripping.

As stack pressures tend to zero, very little net propagation occurs, Fig. 4a. The dendrite length oscillates during plating and stripping, indicating that the cell can be cycled more extensively

before failure. To demonstrate this, three-electrode Li/Li_6PS_5Cl cells were assembled, as described in Methods, and plated at 4.0 mA/cm^2 under stack pressures of 0.1 MPa (ambient) and 7 MPa, Fig 4c & d, respectively. The cells were cycled until short-circuit. A drop in voltage at the end of plating was observed in the first few cycles at both stack pressures, consistent with previous work indicating an increase in contact area as Li penetrates the electrolyte. The cell under ambient pressure achieved a 5-fold increase in the number of cycles corresponding to 170 cycles, Fig 4c, compared with the cell under 7 MPa stack pressure, which short-circuited on the 35th cycle. The effect of pressure on short circuit is further verified at higher pressures and by quantifying amount of capacity passed (Li deposited) to short circuit on a single plating, Figs S14 and S16 respectively. In both figures higher pressures lead to earlier short circuit. Kinzer et al[26], demonstrated critical currents of multiple hundreds of mA/cm^2 when using a molten Li anode due to the vastly improved viscoplasticity of the metal anode as well as a lack of applied stack pressure. Similarly, low temperatures decrease the viscoplasticity of Li and lead to early cell failure as shown in Figure S17 where the same experiment as in Fig 4d was carried out but at 0^{o}C with the cell failing after only 17 cycles. Of course, current density as well as capacity play a role in the pressure dependence of short-circuits, as seen in recent studies of stack pressure effects on Li dendrites in solid electrolytes[27–29]. For example, if sufficiently low current densities are used it is possible to sustain cycling under several MPa pressure[4,29].

To focus on the fundamental understanding of dendrites all cells contained Li metal electrodes in the pristine state. Anodeless conditions and cycling efficiencies would require a separate study.

Implications

Li dendrites and short-circuits can be suppressed by inhibiting either the initiation or propagation of cracks in the solid electrolyte, and the means of doing so differ. For a sintered Li_6PS_5Cl argyrodite electrolyte, using measurements of the microscopic (grain boundary) fracture strength, pore size and population density, a critical current for initiation of ~1.0 mA/cm^2 was calculated. The experimentally reported range is 0.5-3 mA/cm^2 refs[4,23]. Previous efforts have often sought to increase the critical current by raising the macroscopic fracture

toughness of the electrolyte to prevent dendrite initiation. Future strategies should consider local fracture strength. Also, lowering pore size and minimising the number of isolated subsurface pores will increase the critical current for dendrite initiation. Even if dendritic crack initiation cannot be avoided, it is possible to prevent short-circuit for many cycles, by suppressing crack propagation or by limiting the net growth of Li dendrites inside existing dry cracks. Crack propagation depends on the electrolyte's macroscopic fracture toughness, the current density, stack pressure and maximum length a Li dendrite attains in the crack during a given plating step. Even if the same capacity is plated and stripped, stack pressure results in net lengthening of Li within a dry crack per cycle. Low stack pressures minimise dendrite lengthening and mitigate crack propagation. Cells at stack pressures closer to atmospheric can deliver larger numbers of cycles without Li reaching the counter electrode. A Li/Li_6PS_5Cl cell plated at 4.0 mA/cm^2 under 7MPa stack pressure short-circuited after only 35 cycles, whereas a cell at the same current could sustain a 5-fold increase in cycling, not short-circuiting until the 170^{th} cycle under atmospheric pressure. This demonstrates the detrimental effect of pressurising Li anodes during charging.

In practical cells, pressures can result from sources other than stack pressure, e.g., intercalation cathodes may produce significant internal stresses during charge and discharge at high rates. Our model of dendrites not only separates initiation from propagation, but the propagation part of the model also explains how, if stresses in the cell induce cracking of the electrolyte and lithium metal finds its way into such pre-existing cracks, the cracks would propagate and induce failure. Low pressures can result in void formation on stripping[4]. Nevertheless, the basic mechanism of initiation and propagation on plating are expected to be similar, the voiding will lower the contact area and raise the local currents. The desirability of low pressures to suppress dendrite propagation may be incompatible with mitigating voiding, although of course practical cells will have to operate at low stack pressures in any case. Ultimately any practical solid electrolyte will be tens of microns in thickness, although the electrolytes used in this study are ~1mm we anticipate similar basic processes will occur in thinner electrolytes, even though the dimensions of the features involved (cracks, pores, grain size) will be smaller. Whilst smaller features may reduce the J-integral other factors such as more constrained flow of Li metal within smaller features may increase it. Which wins would depend on the details of the materials and operating conditions.

An interesting recent paper has suggested that small aspect ratio Li anodes may exhibit different mechanical properties, including creep and flow[30]. This might depend on the adhesion of Li to the specific SE, in that case LLZO. We have not seen evidence of this in our results, which may be due to a different SE or conditions used. Different solid electrolytes will differ in their microstructure (grain size, pore size, pore population density) and mechanical properties (fracture toughness and local fracture strength), the latter especially when comparing oxides with sulphides or halides. As a result, the values of these parameters will vary, however we anticipate the fundamental mechanism of initiation and propagation described here to apply. Li_6PS_5Cl forms a self-limiting SEI of < 250 nm in contact with Li metal[31]. The pores where dendrites initiate are deeper within the solid electrolyte (pores very near the surface would not build sufficient pressure to initiate dendrites). Therefore, the main effect of a SEI is likely to be confined to the density of microcracks connecting the anode with the sub-surface pores. Where current density is sufficiently low that Li fills the entire length of the crack before reaching the critical length for crack propagation, the mode of cracking will likely switch to Li-tip driven mechanisms of the type described previously[5,9]. Therefore, the present study offers a unified view of dendrites in ceramic electrolytes. Future studies should investigate the consequences of the results reported here, including increasing local fracture strength at the grain boundaries and whether low pressures at the Li anode can be maintained in practical cells leading to higher critical currents and extended cycling.

References

1. Janek, J. & Zeier, W. G. A solid future for battery development. *Nat. Energy* **1**, 16141 (2016).

2. Famprikis, T., Canepa, P., Dawson, J. A., Islam, M. S. & Masquelier, C. Fundamentals of inorganic solid-state electrolytes for batteries. *Nat. Mater.* **18**, 1278–1291 (2019).

3. Ning, Z. *et al.* Visualizing plating-induced cracking in lithium-anode solid-electrolyte cells. *Nat. Mater.* **20**, 1121–1129 (2021).

4. Kasemchainan, J. *et al.* Critical stripping current leads to dendrite formation on plating in lithium anode solid electrolyte cells. *Nat. Mater.* **18**, (2019).

5. Feldman, L. A. & De Jonghe, L. C. Initiation of mode I degradation in sodium-beta

alumina electrolytes. *J. Mater. Sci.* **17**, 517–524 (1982).

6. Porz, L. *et al.* Mechanism of Lithium Metal Penetration through Inorganic Solid Electrolytes. *Adv. Energy Mater.* **7**, 1–12 (2017).

7. Bucci, G. & Christensen, J. Modeling of lithium electrodeposition at the lithium/ceramic electrolyte interface: The role of interfacial resistance and surface defects. *J. Power Sources* **441**, 227186 (2019).

8. Klinsmann, M., Hildebrand, F. E., Ganser, M. & McMeeking, R. M. Dendritic cracking in solid electrolytes driven by lithium insertion. *J. Power Sources* **442**, 227226 (2019).

9. Barroso-Luque, L., Tu, Q. & Ceder, G. An Analysis of Solid-State Electrodeposition-Induced Metal Plastic Flow and Predictions of Stress States in Solid Ionic Conductor Defects. *J. Electrochem. Soc.* **167**, 20534 (2020).

10. Zhou, L. *et al.* High areal capacity, long cycle life 4 V ceramic all-solid-state Li-ion batteries enabled by chloride solid electrolytes. *Nat. Energy* **7**, 83–93 (2022).

11. Koç, T., Marchini, F., Rousse, G., Dugas, R. & Tarascon, J.-M. In Search of the Best Solid Electrolyte-Layered Oxide Pairing for Assembling Practical All-Solid-State Batteries. *ACS Appl. Energy Mater.* **4**, 13575–13585 (2021).

12. Liang, J. *et al.* A Series of Ternary Metal Chloride Superionic Conductors for High-Performance All-Solid-State Lithium Batteries. *Adv. Energy Mater.* **n/a**, 2103921 (2022).

13. Tu, Q., Shi, T., Chakravarthy, S. & Ceder, G. Understanding metal propagation in solid electrolytes due to mixed ionic-electronic conduction. *Matter* **4**, 3248–3268 (2021).

14. Kazyak, E. *et al.* Li Penetration in Ceramic Solid Electrolytes: Operando Microscopy Analysis of Morphology, Propagation, and Reversibility. *Matter* **2**, 1025–1048 (2020).

15. Scharf, J. *et al.* Bridging nano- and microscale X-ray tomography for battery research by leveraging artificial intelligence. *Nat. Nanotechnol.* (2022). doi:10.1038/s41565-022-01081-9

16. De Jonghe, L. C., Feldman, L. & Beuchele, A. Slow degradation and electron conduction in sodium/beta-aluminas. *J. Mater. Sci.* **16**, 780–786 (1981).

17. Han, F. *et al.* High electronic conductivity as the origin of lithium dendrite formation within solid electrolytes. *Nat. Energy* **4**, 187–196 (2019).

18. Masias, A., Felten, N., Garcia-Mendez, R., Wolfenstine, J. & Sakamoto, J. Elastic, plastic, and creep mechanical properties of lithium metal. *J. Mater. Sci.* **54**, 2585–2600 (2019).

19. Sedlatschek, T. *et al.* Large-deformation plasticity and fracture behavior of pure lithium under various stress states. *Acta Mater.* **208**, 116730 (2021).

20. Doltsinis, I. & Dattke, R. Modelling the damage of porous ceramics under internal pressure. *Comput. Methods Appl. Mech. Eng.* **191**, 29–46 (2001).

21. Foulk J.W., I. I. I., Johnson, G. C., Klein, P. A. & Ritchie, R. O. On the toughening of brittle materials by grain bridging: Promoting intergranular fracture through grain angle, strength, and toughness. *J. Mech. Phys. Solids* **56**, 2381–2400 (2008).

22. Monroe, C. & Newman, J. Dendrite Growth in Lithium/Polymer Systems: A Propagation Model for Liquid Electrolytes under Galvanostatic Conditions. *J. Electrochem. Soc.* **150**, A1377 (2003).

23. Liu, G. *et al.* Densified Li6PS5Cl Nanorods with High Ionic Conductivity and Improved Critical Current Density for All-Solid-State Lithium Batteries. *Nano Lett.* **20**, 6660–6665 (2020).

24. Begley, J. A. & Landes, J. D. The J Integral as a Fracture Criterion. *ASTM STP* **514**, 1–2 (1972).

25. Huang, Z. & Li, X. Origin of flaw-tolerance in nacre. *Sci. Rep.* **3**, 1693 (2013).

26. Kinzer, B. *et al.* Operando analysis of the molten Li|LLZO interface: Understanding how the physical properties of Li affect the critical current density. *Matter* **4**, 1947–1961 (2021).

27. Lewis, J. A. *et al.* Role of Areal Capacity in Determining Short Circuiting of Sulfide-Based Solid-State Batteries. *ACS Appl. Mater. Interfaces* **14**, 4051–4060 (2022).

28. Hänsel, C. & Kundu, D. The Stack Pressure Dilemma in Sulfide Electrolyte Based Li Metal Solid-State Batteries: A Case Study with Li6PS5Cl Solid Electrolyte. *Adv. Mater.*

Interfaces **8**, 2100206 (2021).

29. Doux, J.-M. *et al.* Stack Pressure Considerations for Room-Temperature All-Solid-State Lithium Metal Batteries. *Adv. Energy Mater.* **10**, 1903253 (2020).

30. Haslam, C. G., Wolfenstine, J. B. & Sakamoto, J. The effect of aspect ratio on the mechanical behavior of Li metal in solid-state cells. *J. Power Sources* **520**, 230831 (2022).

31. Otto, S.-K. *et al.* In Situ Investigation of Lithium Metal–Solid Electrolyte Anode Interfaces with ToF-SIMS. *Adv. Mater. Interfaces* **9**, 2102387 (2022).

ACKNOWLEDGEMENTS

P.G.B. is indebted to the Faraday Institution SOLBAT (FIRG007, FIRG008, FIRG026), as well as the Engineering and Physical Sciences Research Council, Enabling Next Generation Lithium Batteries (EP/M009521/1), the University of Oxford experimental equipment upgrade (EP/M02833X/1) and the Henry Royce Institute for Advanced Materials (EP/R0066X/1, EP/S019367/1, EP/R010145/1) for financial support. We thank Diamond Light Source, Harwell, United Kingdom, for provision of synchrotron radiation beam time (experiment no. MG23980-1) at the I13-2 beamline of the Diamond Light Source. We acknowledge technical and experimental support at the I13-2 by Andrew Bodey.

Author Contributions:

Z.N., G.L. and D.L.R.M. contributed to all aspects of the research. Z.N., D.L.R.M., D.S.J., S.D.P., G.O.H., and A.B. carried out the operando synchrotron XCT. Z.N. and D.L.R.M. performed the preparation of electrolyte disks and cell assembly. Z.N., D.L.R.M, C.G. and X.G. performed the On-line mass spectrometry. Z.N., D.L.R.M, B.H, B.L and J.B. performed the Plasma FIB imaging. D.L.R.M and J.B. performed Plasma FIB imaging with SIMS. Z.N., D.L.R.M., J.P., J.L. and D.E.J.A. conducted the preparation of micro-cantilever and mechanical tests. G.L., Y.C. and C.W.M. conducted the modelling. Z.N., G.L., D.L.R.M., D.S.J., R.I.T., P.S.G., D.E.J.A., T.J.M., C.W.M. and P.G.B. discussed the data. All authors contributed to the interpretation of data. Z.N., D.L.R.M., G.L., C.W.M. and P.G.B. wrote the manuscript with contributions and revisions from all authors. The project was supervised by C.W.M., T.J.M. and P.G.B.

Data Availability:

The datasets generated during and/or analysed during the current study are available from the corresponding author on reasonable request.

Code availability:

The computer code generated and used during the current study is available from the corresponding author on reasonable request.

Ethics declarations:

The authors declare no competing interests

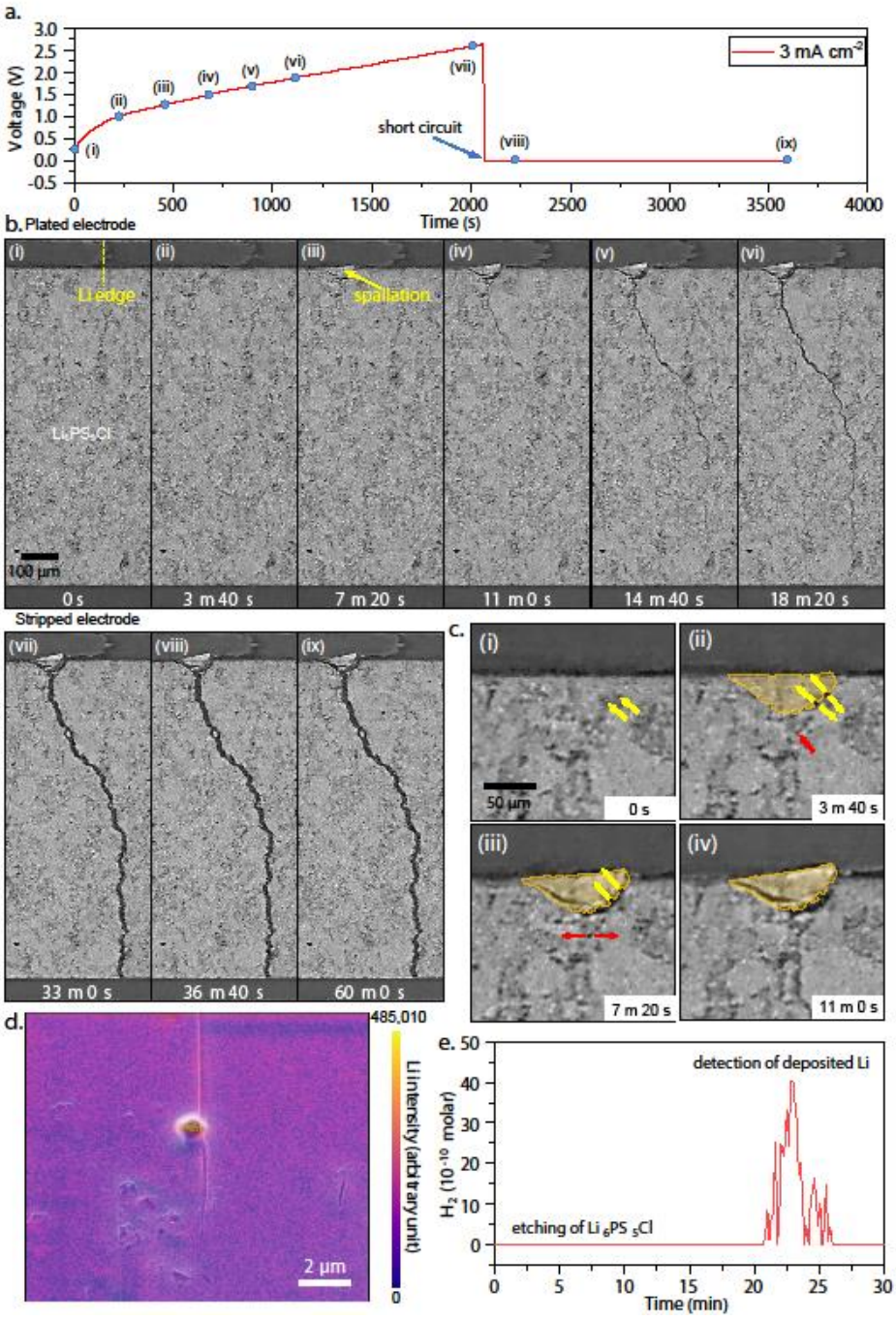

Fig 1. Operando XCT virtual cross-sections during plating of a Li/Li_6PS_5Cl/Li cell showing the development of a dendrite crack from initiation through propagation to complete short-circuit. Combined FIB-SEM with SIMS as well as mass spectrometry provide evidence supporting the presence of Li in sub-surface regions of the solid electrolyte. **a.** Voltage versus time for a Li/Li_6PS_5Cl/Li cell, plated at a current density of 3 mA/cm^2 to a capacity of 3 mAh/cm^2 under 7 MPa stack pressure. The points indicate times at which XCT scans, shown in **b**(i)–(ix), terminated. **b.** Virtual cross-sectional image slices reveal the growth of a crack through an initially pristine electrolyte. A dendrite initiates at the lithium-plating (top)

surface (i)-(iii), forming a transverse crack that propagates until the cell short circuits (iv)-(viii), see also Video S1. **c.** Magnified images of the region near the plated electrode in **b**; pristine (i) and after successive plating (ii)-(iv), showing formation of the spallation and transverse crack. Yellow arrows indicate pores associated with forming the spallation, and red arrows indicate pores associated with propagation of the transverse crack. The spalled-out solid electrolyte is shaded in yellow to illustrate its movement. **d.** FIB-SEM image of a subsurface pore within a Li_6PS_5Cl electrolyte disk after plating. The corresponding Li^+ SIMS mapping is overlayed demonstrating the presence of Li metal in the subsurface pore. **e**. Detection of H_2 in the gas phase from a Li_6PS_5Cl solid electrolyte disk etched with excess LiOH solution after Li plating and removal of the electrodes; the delayed response indicates Li deposition primarily in the sub-surface region of the electrolyte, see also Fig S9.

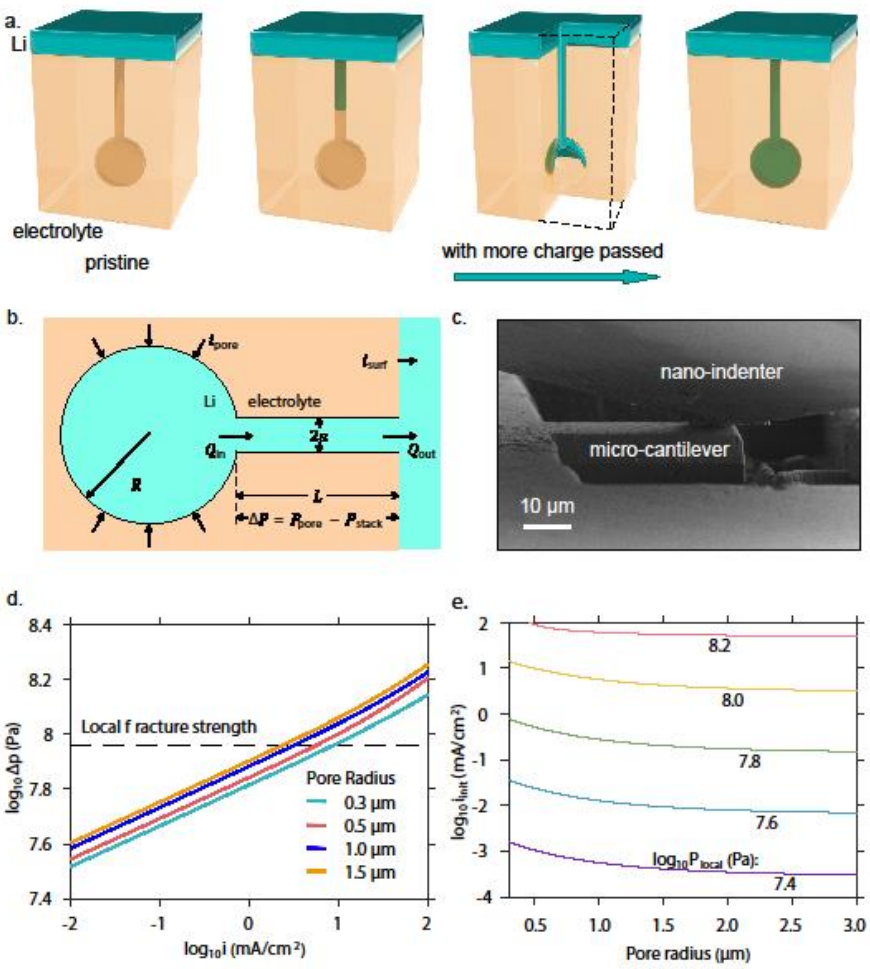

Fig 2. Schematics and implications of the dendritic crack initiation process. Higher current density leads to greater pressure in the pore, with cracking occurring when the pressure

exceeds the local (grain boundary) fracture strength of the solid electrolyte. **a.** Schematic of a pore connected to the lithium/solid-electrolyte interface through a microcrack and being filled by Li deposition. **b.** A schematic of the filled subsurface pore/microcrack system, labelled with parameters relevant to the dendrite initiation model: P_{stack} is the stack pressure on the cell. During constant-current charging, Li is plated with a current density of i_{surf}, while the pore interior experiences a different current density i_{pore}. Because the lithium is incompressible and ductile, i_{pore} induces extrusion of lithium towards the surface. As a consequence of this current-induced lithium extrusion, a pressure, P_{pore}, builds up within the pore in excess of the stack pressure P_{stack}. The pore population density was used to calculate i_{pore} and i_{surf} (see Fig S2 and Fig S11) **c.** SEM image depicting the measurement of local fracture strength by microcantilever bend tests, see also Methods and Fig S19. **d.** The dependence of hydrodynamic pressure in the pore on current density, for various pore radius: 1.5 µm (orange), 1.0 µm (blue), 0.5 µm (red) and with no pore, i.e., a microcrack that terminates with a hemispherical tip, *R* = *a*, where *a* is 300 nm (turquoise). For simulations, the microcrack length *L* was 5 µm and the separation distance between pores was 10 µm (see Fig S11). The horizontal dashed line shows the local fracture strength of the electrolyte determined by the microcantilever experiments. **e.** Plot showing how the critical current density for crack initiation varies with pore size for different local fracture strengths.

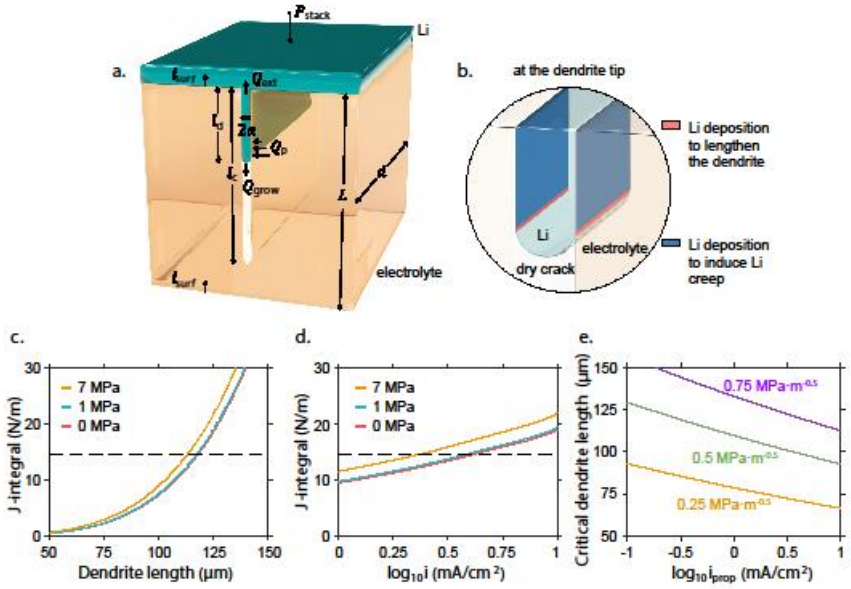

Figure 3. Dendrite crack propagation. Longer Li dendrites, higher currents and greater

stack pressures promote crack propagation. Li dendrites do not need to fill a crack completely to meet the fracture criterion required for crack lengthening. a. Schematic of a planar dendritic crack: length l_c and width $2a$, partially filled by a Li dendrite of length l_d. Cell stack pressure of P_{stack}. Li plating takes place at all Li/electrolyte interfaces. Li deposition where the crack surface is in contact with the metal, blue region in **b,** drives viscoplastic flow that causes an extrusion flux Q_{ext} back into the bulk Li at the dendrite's base and a flow Q_{grow} that extends the Li dendrite further within the dry crack. Deposition at the three-phase contact line where Li, electrolyte, and free space meet, red region in **b**, contributes directly to lengthening of the Li dendrite. **c.** J-integral at the crack tip as a function of dendrite length. **d** J-integral at the crack-tip as a function of the current density for Li plating (dendrite length l_d = 115 µm). **e.** The effect of fracture toughness on applied current density and lithium dendrite length required to lengthen a dry crack (shown for a 200 µm long dry crack and zero stack pressure).

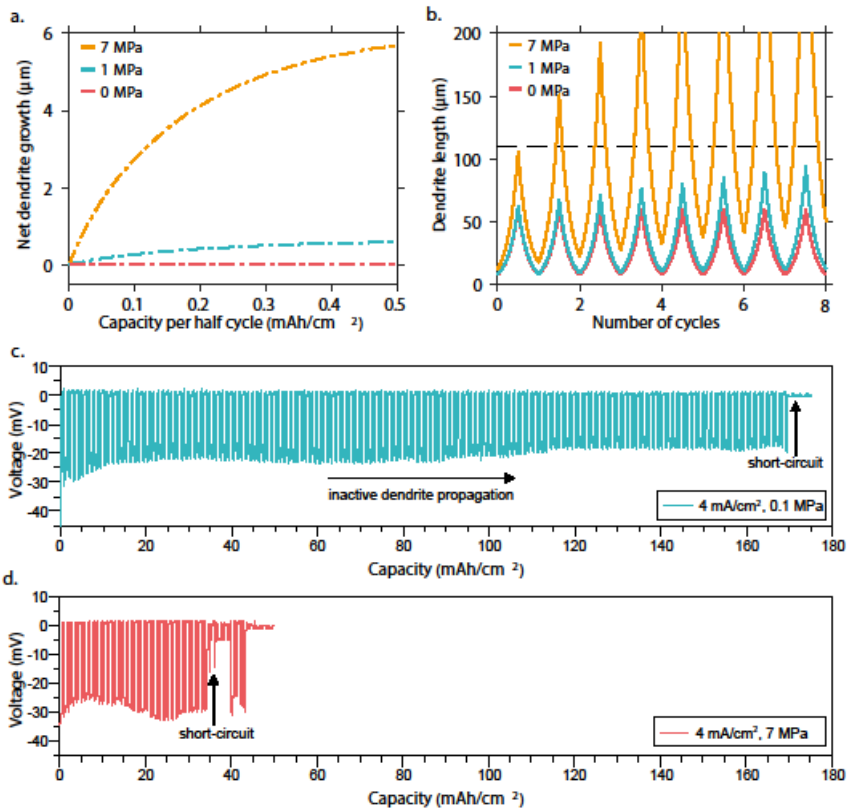

Fig 4. Propagation of a Li dendrite under various stack pressures. Larger stack pressures reduce the number of cycles to short circuit. Removal of applied stack pressure can enable prolonged cycling. a. The net change in Li dendrite length within the crack on one charge–

discharge cycle as a function of capacity under various stack pressures. **b**. Cumulative dendrite length during cell cycling under various stack pressures. As stack pressures reduce the net lengthening of the Li dendrite per cycle tends to zero, inhibiting both crack propagation and short-circuiting by the dendrite **c**. & **d**. Cycling of Li/Li_6PS_5Cl 3-electrode cell with current densities of 4.0 mA/cm^2 for plating, 0.05 mA/cm^2 for stripping (to avoid void formation), both for a capacity of 0.5 mAh/cm^2, under ambient pressure (0.1 MPa) (**c**) and 7 MPa pressure (**d**).

Methods

Electrolyte preparation and cell assembly

All procedures were performed inside an Ar-filled glove box (O_2 and H_2O levels < 1 ppm). Li_6PS_5Cl solid electrolyte powder with a particle size of D50 ~ 10 µm was purchased from *MSE Supplies* and pressed into a disk with a 5-mm-diameter stainless steel die set under a uniaxial pressure of 400 MPa. The disk was then transferred to a furnace and sintered at 300 ℃ for 20 min. The sintered electrolyte disk was then cooled to room temperature and used for cell assembly. For *Operando* XCT characterisation, metallic lithium 100 µm thick was punched into 2-mm-diameter disk-shaped lithium electrodes and pressed onto both sides of the sintered Li_6PS_5Cl disk. The cell was then assembled into a customised tube-cell, which maintained airtightness and a stack pressure of 7 MPa on the beamline.

Three-electrode cell cycling

For a three-electrode cell, two disk-shaped lithium electrodes of 1 mm diameter were pressed onto the same side of the electrolyte disk as the working and reference electrodes. The working and reference electrode were separated by a 1 mm-wide polymer insulating tape mask. A 5 mm lithium disk was pressed onto the other side as the counter electrode. The assembly was then placed into a pouch cell, and sealed under vacuum (~ 10^{-3} bar). Poor Li/SE contact can lead to increased critical current densities with increasing pressure just because the contact improves with pressure. Therefore, establishing and retaining good contact at the Li/SE is important when investigating fundamental mechanism of dendritic failure[27–29]. Therefore, a high forming pressure was used to ensure a good Li/Li_6PS_5Cl contact (see FIB-SEM Figure S18). The cells were cycled galvanostatically with a capacity on each half-cycle of 0.5 mAh/cm^2. While the plating current on the working electrode was 4 mA/cm^2, a current density of 0.05 mA/cm^2 was used on stripping to ensure no void formation at the WE/SE

interface. All galvanostatic measurements were performed using a Gamry Interface 1010 potentiostat.

Operando X-ray computed tomography

X-ray tomograms were recorded at the I13-2 beamline at the Diamond Light Source. A pink beam with beam energy ranging from 8 keV to 30 keV was employed to maximise the X-ray beam flux and so improve the time resolution. Projections were collected with a PCO Edge 5.5 sCMOS camera combined with an optical microscope with a ×4 magnification, resulting in a pixel size of 1.625 µm and a field of view of 4.7 × 4.4 mm^2. A 500-µm-thick LuAG scintillator was used to convert X-rays to visible light. The exposure time was set to 100 ms. For each tomogram, 1801 equiangularly distributed projections were taken over 180º as well as 50 dark and 50 flat references before and after the whole *operando* experiment. X-ray tomograms were obtained at the pristine state, and were then collected continuously during galvanostatic plating with a current density of 3 mA/cm^2 and a capacity of 3 mAh/cm^2. During the galvanostatic plating 7 MPa of pressure was applied using a constantly applied spring force which was measured and calibrated using a transducer. A final tomogram was collected at the end of plating.

On-line Mass Spectrometry (OMS)

OMS measurements were conducted on pristine and Li-plated Li_6PS_5Cl. Sintered Li_6PS_5Cl disks were placed between Li electrodes and Li plated galvanostatically at a current density of 0.05 mA/cm^2 and a capacity of 2 mAh/cm^2. A second cell was assembled identically and no current was passed. The cells were then disassembled, the lithium electrodes removed including with finely polished 4000-grid polishing papers in an Ar-filled glovebox. The solid electrolyte disks were then transferred into a sealed vial along with a magnetic stirrer. An excess amount of degassed aqueous LiOH solution was then injected into the vial, slowly dissolving the Li_6PS_5Cl electrolyte and reacting with any Li metal inside the electrolyte evolving H_2. The released H_2 was detected and quantified by the mass spectrometer (Prima BT, Thermo Fisher Scientific) as a percentage of the total gas flow.

Plasma FIB-SEM

A 5 mm pristine Li_6PS_5Cl disk was transferred into the chamber of the PFIB-SEM (Thermo Fisher Helios G4 Plasma-FIB Dualbeam) for FIB milling with an ILoad vacuum sample transfer system without exposure to air. The freshly milled cross-section was then imaged with SEM to visualise the pores and micro-cracks in proximity to the interface.

Secondary Ion Mass Spectrometry

A 5mm Li_6PS_5Cl disk which had undergone a single plating at 0.05 $mA.cm^{-2}$ for 5 $mAh.cm^{-2}$ was imaged using the PFIB-SEM procedure above. SIMS analysis was performed on the cross-section using a Hidden Analytical EQS quadrupole SIMS detector. A focussed beam of Xe^+ was used for SIMS analysis. The quadrupole detector was tuned to collect the $^7Li^+$ signal.

Nanoindentation: Elastic Modulus, Hardness and Fracture Toughness

In-situ nanoindentation and micro cantilever bending (Hysitron PI 88) within a TESCAN scanning electron microscope enabled measurement of air sensitive Li_6PS_5Cl disks without the need for mineral oil or other techniques that can affect the mechanical response[32]. Samples were transferred to the SEM within an airtight transfer container. Indentation modulus and hardness were calculated using the Oliver-Pharr method[33] on multiple indents made with a Berkovich tip. Further details in the Supplementary Information.

For the determination of fracture toughness, a cube corner tip was used to cause fracture of the electrolyte. Using the Lawn, Evans, and Marshall equation (Eq. 1) the fracture toughness, K_{1C}, was calculated for each of the multiple indents. Where E is modulus, H is hardness, P is load, c is total crack length and α is a geometric constant for a cube corner tip. The average across all indents was taken as the Li_6PS_5Cl fracture toughness.

$$K_{1C} = \alpha \left(\frac{E}{H}\right)^{1/2} \left(\frac{P}{c^{3/2}}\right) \qquad \text{(Equation 1)}$$

The standard protocols for determining fracture toughness were followed, based on references 65 and 66[34,35], including ensuring minimal pile-up as shown in Figure S21. Further details are available in the Supplementary Information.

Microcantilever Bending: Local Fracture Strength

Microcantilevers were produced using a Thermo Scientific Helios G4 Plasma FIB DualBeam (or PFIB) system combined with an ILoad vacuum sample transfer system. The preparation of

microcantilevers using the FIB milling method is described in detail in previous work[36]. Loading was performed using a cube corner tip, in a displacement-controlled regime, at a rate of 2.5 nm per second until fracture occurred. The grain boundary strength σ_c for each microcantilever was calculated using the following equation for the tensile surface stress:

$$\sigma_c = \frac{P_f L_C y}{I}$$

Where P_f is load at the point of fracture, L_C is the distance between loading point and crack, I is the second moment of area and y is the vertical distance between the neutral plane and the upper surface. I and y were calculated for a pentagonal beam as shown by Chen et al.[37]. Three microcantilevers were tested and the mean value of the tensile surface stress at failure was taken for local fracture strength of the Li_6PS_5Cl.

Additional References

32. Baranowski, L. L., Heveran, C. M., Ferguson, V. L. & Stoldt, C. R. Multi-Scale Mechanical Behavior of the Li3PS4 Solid-Phase Electrolyte. *ACS Appl. Mater. Interfaces* **8**, 29573–29579 (2016).

33. Oliver, W. C. & Pharr, G. M. Measurement of hardness and elastic modulus by instrumented indentation: Advances in understanding and refinements to methodology. *J. Mater. Res.* **19**, 3 (2004).

34. Zhang, T., Feng, Y., Yang, R. & Jiang, P. A method to determine fracture toughness using cube-corner indentation. *Scr. Mater.* **62**, 199–201 (2010).

35. Cuadrado, N., Casellas, D., Anglada, M. & Jiménez-Piqué, E. Evaluation of fracture toughness of small volumes by means of cube-corner nanoindentation. *Scr. Mater.* **66**, 670–673 (2012).

36. Di Maio, D. & Roberts, S. G. Measuring fracture toughness of coatings using focused-ion-beam-machined microbeams. *J. Mater. Res.* **20**, 299–302 (2005).

37. Chen, Y. *et al.* Measurements of elastic modulus and fracture toughness of an air plasma sprayed thermal barrier coating using micro-cantilever bending. *Surf. Coatings Technol.* **374**, 12–20 (2019).